Soft Matter



PAPER View Article Online
View Journal | View Issue



Cite this: *Soft Matter,* 2019, **15**, 6485

Received 18th June 2019, Accepted 19th July 2019

DOI: 10.1039/c9sm01212e

rsc.li/soft-matter-journal

Control of formation of viscoelastic droplets and distribution of nano-inclusions in functional deposition for lithium—sulfur batteries

Mounica J. Divvela, Rui Zhang, Yevgen Zhmayev, Shubham Pinge, Jin Hong Lee, Seung Wan Kim and Yong Lak Joo®*

The electrospray process produces micro/nanodroplets for various applications such as thin and uniform coatings, drug carriers and mass spectrometry. In this paper, we study the spray processes of viscoelastic jets using simulations and experiments. In discretized modeling, the jet is perturbed with axisymmetric instability and the growth of this instability causes the jet to break into droplets. For the experiments, a solution of polyvinyl alcohol in water is sprayed and is visualized using a high-speed camera. The droplet size distribution is studied from simulations with experiments for three spray cases: electrospray, air spray, and air-controlled electrospray. Our simulations and experiments reveal that the electric field is effective in reducing the droplet size, while air flow offers more jet break-ups and thus a larger number of droplets. As a result, air-controlled electrospray where these two driving forces are synergistically combined leads to a larger number of smaller droplets than electrospray or air spray. Finally, we applied three spray processes to obtain a deposition of sulfur/mesoporous carbon/graphene/ polymer binder composites as a lithium sulfur battery cathode and demonstrated that air-controlled electrospray leads to a higher capacity and rate capability than other processes, exhibiting 800 mA h $\rm g^{-1}$ at 0.5C and 600 mA h $\rm g^{-1}$ at 2C.

1. Introduction

The electrospray process is used to produce electrically charged droplets of size in the micron and submicron range. This process is used in diverse applications such as production of thin and uniform coatings, nanodroplet and nanostructure production, biomedical engineering, energy storage and mass spectrometry. 1-10 In this process, the electrospraying liquid is pumped out of the needle through a syringe and an electric field is applied between the needle and the collecting plate. When the liquid is released out of the needle the electric field causes the charges to separate inside the liquid meniscus and it takes the shape of a cone at the needle tip, and is called the Taylor cone. 11 When the Taylor cone becomes unstable, depending on the process conditions either jets or droplets are ejected from the cone. 11-14 The axisymmetric instability of the jet results in modulations in the radius of the jet. There have been several classical studies on the mode of instability by Plateau and Rayleigh¹⁵ who have studied the onset of the instability on a free-falling stream.

In the spray process for viscoelastic jets, the jet extends due to viscoelastic forces and the axisymmetric instability acts on the jet before the break-up. However, in non-viscoelastic liquids, the atomization of the meniscus at the nozzle is responsible for the formation of droplets. In the electrospray process, the electric field force is responsible for the growth of the instability and the jet breaks into droplets. ^{16–18} In the air spray process, an external air flow is applied axially to the jet and the air drag accelerates the growth of the axisymmetric instability. In the current work, we look at spray phenomena in the following cases: (i) electrospray (only electric field), (ii) air spray (only airflow) and (iii) air controlled electrospray (airflow and electric field).

There are several theoretical studies on the shape of the Taylor cone and electrically driven viscoelastic polymer jets^{16–24} but there are few theoretical studies on the jet breakup and droplet dynamics in the electrospray process. Among the studies on electrically driven droplets, there have been separate theoretical studies on: (i) capillary jet breakup under an electric field force, ^{25,26} and (ii) the dynamics of the droplets formed under an electric field. ^{27,28} However, there is no theoretical model combining these two phenomena, as both together are responsible for the electrospray process. Therefore, this work focuses on the breakup of the jet into droplets due to the increase in the growth of the axisymmetric instability, and the dynamics of the droplets as they reach the collecting plate.

Robert Frederick Smith School of Chemical and Biomolecular Engineering, Cornell University, Ithaca, NY, 14853, USA. E-mail: ylj2@cornell.edu Paper Soft Matter

Combining these two phenomena is difficult with the Eulerian approach as there is discontinuity in the equations of motion as we shift from the jet regime to the droplet regime. Therefore, in this work, we use a Lagrangian discretized model as it is suitable for modeling both the jet breakup and droplet dynamics. ^{18,24,29,30}

In the discretized model, we consider the liquid jet to be made up of a series of beads attached together with springs. Newton's second law of motion is applied to conserve the momentum. This model has been used in our previous studies on centrifugal spinning, and axisymmetric and bending instability studies in the electrospinning process. 18,24,29,30 We extend our previous axisymmetric instability¹⁸ work to study the break-up of the jet, which is responsible for the formation of droplets during the electrospray process. In addition, we incorporate equations of motion for the formed droplets to study their dynamics. In this model, we also model the spray process due to external air flow by incorporating the air drag effects for air spray and air controlled electrospray cases. We also conducted experiments for 5 wt% polyvinyl alcohol in water. The air spray, electrospray, and air controlled electrospray processes are visualized using a high-speed camera. The average radius of the droplets obtained from experiments is compared with the simulation results. The surface roughness and efficiency of the coating of PVA/H2O solution on the collector are determined to study the effect of the air flow rate on the air controlled electrospray of the solution. We further investigated the effect of additional deformation on the deposition homogeneity and the dispersion of carbon NPs (carbon black) in the resulting coatings, as it plays a crucial role in energy-storage applications. In addition, we also studied the air controlled electrospray of the solution of graphene oxide dispersion in water to understand the behavior of nano-inclusions in the spray process. Finally, we used the air controlled electrospray process to fabricate cathodes with microporous structures for application in lithium sulfur batteries. With the application of the air controlled electrospray technique, it is possible to control the morphology of cathodes by changing spray parameters and obtain a uniform coating with high sulfur loading. Also, higher sulfur utilization can be achieved through improved electron transfer from low polarization and fast redox reaction kinetics.

2. Electrospray experiments

2.1 Experimental fluids

The spraying solution is 5 wt% of polyvinyl alcohol (PVA) $(M_{\rm w}=25\,000~{\rm g~mol^{-1}})$ in deionized water. 88% mole hydrolyzed polyvinyl alcohol was purchased from Polysciences, Inc. The material properties and model parameters of the spinning solution (PVA & water solution) are shown in Table 1. The viscosity and relaxation times were determined using a TA Instruments AR2000 Rheometer with a 20 mm cone steel plate geometry.

A dispersion study of the coating was performed with electrospray and AC electrospray of 3 wt% PVA/H₂O solution with 15 vol% carbon black. Carbon black (CB) was provided by

Table 1 Material properties and parameters for the Giesekus model for 5 wt% of PVA and H_2O solution

Properties	Value
Density (kg m ⁻³)	964.5
Solution viscosity (Pa s)	0.026
Surface tension (N m ⁻¹)	0.00538
Relaxation time, λ (s)	0.16
Mobility factor, α	0.1
Polymer/solution viscosity ratio, β	0.2

TIMCAL Graphite & Carbon Super $P^{\mathbb{R}}$ Conductive. The graphene oxide solution (2 wt% in water) was obtained from Dongjin Semichem. The graphene oxide solution was further diluted to 3 wt% solution in water.

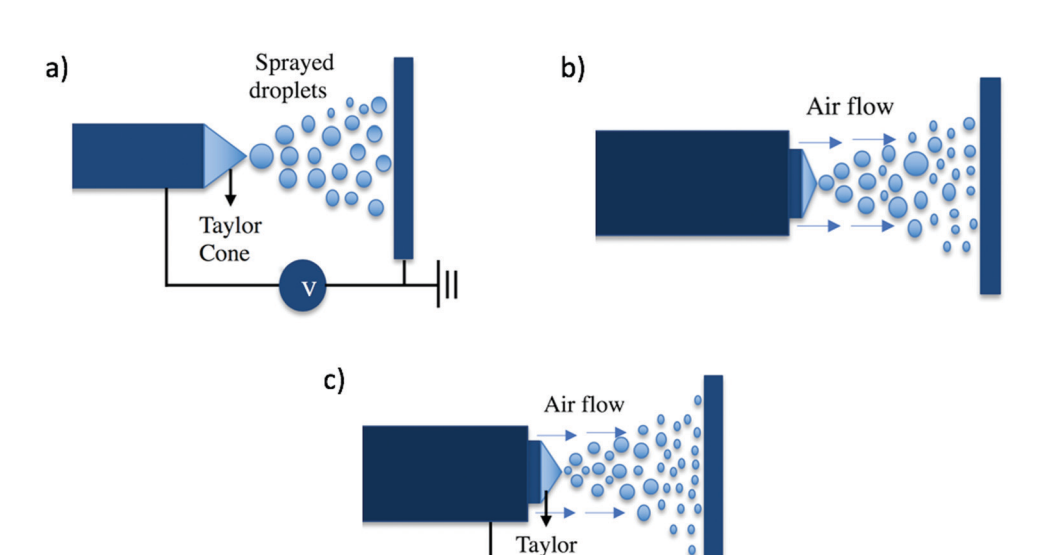
For the preparation of spraying solution for lithium sulfur cathodes, the carbon/sulfur composite was first prepared by grinding 0.336 g sulfur and 0.084 g Ketjen black (AkzoNobel) together and heating at 155 °C for 12 hours to ensure sulfur impregnation. Then the composite was mixed with 0.06 g PAA ($M_{\rm w}=450\,000$ g mol⁻¹, Sigma Aldrich) and 2 g of 6 wt% graphene water solution (ACS Nano). Finally, the mixture was dispersed in 2:8 weight ratio of isopropanol and water to form 6 wt% solution.

2.2 Experimental setup

The experimental setup for electrospraying is shown in Fig. 1. The PVA/ $\rm H_2O$ solution is pumped out of a 16-gauge needle at a flow rate of 0.01 ml min⁻¹ by using a programmable PHS Ultra syringe pump (Harvard Apparatus). The voltage difference in the spinning gap is determined using a Gamma High Voltage Research voltmeter. The experiments are conducted for 7.5, 12.5 and 15 kV voltage differences and the spinning distance is at \sim 16 cm. The spinning behavior of the polymer fiber is visualized using a high-speed camera (RedLake MotionPro HS-3 with Nikon MICRO NIKORR 60 mm 1:2:8 lens). The images are taken at 1000 frames per second. Finally, the images are digitized using MotionStudio x64 software and are analyzed using ImageI.

The coating of 3% PVA/H₂O solution containing 15 vol% carbon black is prepared and sprayed *via* electrospraying and AC electrospraying. The flow rates for electrospraying and AC electrospraying are 0.005 and 0.06 ml min⁻¹ respectively, and the electric field is kept constant at 100 kV m⁻¹ for both processes. Graphene oxide dispersion in water is performed using the AC electrospray process at 0.1 ml min⁻¹ flow rate and 25 kV voltage difference with a spinning distance at 25 cm. The coating morphology and topology are characterized using scanning electron microscopy (Tescan Mira3 FESEM).

Lithium sulfur cathode solution is sprayed onto carbon coated aluminum foil using a coaxial needle (12-gauge inside, 16 gauge outside). The flow rate and distance are kept at $0.05~\rm ml~min^{-1}$ and $10~\rm cm$ respectively. The voltage and air pressure are changed to have electrodes sprayed under no electric field (0 kV/25 psi), no air (25 kV/0 psi) and both the electric field and air (25 kV/25 psi) conditions. Sample cathodes are used in 2032 coin cells with a lithium disk as the anode.



Cone

Fig. 1 Schematic of (a) electrospray, (b) air spray and (c) air controlled (AC) electrospray.

Cycling performances are tested using a battery analyzing station (BTS8-MA, MTI) at 0.2C in a voltage window of 1.8-2.8 V.

3. Discretized model

The electrospinning system is modeled using the bead-spring model; the jet is assumed to be a series of beads attached to each other with springs. The modeling approach is similar to the model used previously in electrospinning and centrifugal spinning systems. ^{18,24,29,30} The polymer jet that is ejected out of the nozzle is subject to axisymmetric instabilities. This instability further leads to breaking of the jet into droplets. The modeling procedure used in this work is according to our previous work on axisymmetric instability. ¹⁸

When the Eulerian frame of reference is used, it is difficult to have one coordinate system as we shift the frame of reference from the continuous flow of the jet to discrete droplets. However, in the Lagrangian model used in the current study, we can incorporate the equations of motion for both, the continuous polymer jet and the droplets. The beads for the jet are connected with viscoelastic springs and when the jet breaks up and forms droplets each droplet is considered as one bead. This model is for predicting the spray process close to the needle so we do not consider the fission of the droplets. Until now all the studies have been conducted separately on either the capillary jet breakup or droplet dynamics but this model incorporates both these phenomena in the electrospray process. ^{25–28}

For the jet, the equations of motion for a bead 'i' of mass m_i , length l_i , and radius r_i are obtained by applying Newton's second law (eqn (1)). The position vector \mathbf{x}_i is obtained from the forces acting on the bead 'i', which are surface tension $F_{\mathrm{st},i}$, viscoelastic force $F_{\mathrm{v},i}$, drag force $F_{\mathrm{d},i}$, electric force $F_{\mathrm{e},i}$ and gravitational force $F_{\mathrm{g},i}$. The effects of solvent evaporation are

not significant and are not considered in the model as we studied the jet behavior close to the nozzle.

$$m_i \frac{\mathrm{d}^2 x_i}{\mathrm{d}t^2} = F_{\mathrm{st},i} + F_{\mathrm{v},i} + F_{\mathrm{d},i} + F_{\mathrm{e},i} + F_{\mathrm{g},i},$$
 (1)

The surface tension force and viscoelastic force are determined according to the work by Divvela *et al.*^{18,24} The surface tension force has two components: (i) capillary force and (ii) bending force due to the local curvature of the jet. The viscoelastic force is due to the stress from the solvent and the polymer; the solvent is a Newtonian fluid, and the polymer stress is obtained from the Giesekus model. The drag force due to the coaxial air flow is determined by considering the average of the drag effects on the upstream and the downstream elements. The drag force has two components: (i) the friction drag due to shear stress on the surface of the jet and (ii) the pressure drag due to pressure difference in the radial direction of the jet.³⁰

The electric force on a bead 'i' is provided in eqn (2). The electric field on the element i has two terms: (i) the voltage gradient with applied voltage difference V_o and spinning length h, and (ii) the coulombic interaction with the rest of the beads j with charge q_j at a distance x_{ij} from bead 'i'. The surface charges are conserved by considering the convection and conduction currents. ¹⁸

$$F_{e,i} = q_i E_{e,i} = q_i \left(\frac{V_o}{h} e_z + \frac{1}{4\pi\varepsilon_0} \sum_{j \neq i} \frac{q_j}{x_{ij}} x_{ij} \right), \tag{2}$$

The bead at the nozzle is disturbed with a normal mode of perturbation with amplitude δ and frequency ω_0 . In the context of axisymmetric instability, our approach is similar to that used in the capillary jet breakup study.^{25,26} In this study, small fluctuations are applied under jet boundary conditions

Paper Soft Matter

at the nozzle. The applied perturbation is given in eqn (3), where a_s is the stable jet radius.

$$a = a_s + \delta e^{\omega_0 t}. (3)$$

The simulation is run for different frequencies and amplitudes of the perturbations as given in eqn (3). This perturbation is applied when the bead is introduced at the nozzle exit and we obtain the jet variables by solving eqn (1). This solution will have information on the stable jet and the perturbed variables combined. We calculate the growth rate ω_r of the instability from eqn (4) by measuring the temporal evolution of the perturbation radius, $a_{\epsilon}(t)$. Finally, we consider the amplitude δ and frequency ω_0 for which we obtain the maximum growth rate.

$$\ln(a_{\varepsilon}(t)) = \omega_{\rm r}t + \ln(a_{\varepsilon}(0)), \tag{4}$$

The amplitude of the instability increases with time and when this amplitude is equal to the radius of the jet, the jet breaks and forms spherical droplets. Therefore, the jet breakup occurs when $a_{\epsilon}(t) = R(t)$, where R(t) is the radius of the jet. The mass, charge, and velocity of the new droplets formed are obtained from conservation of mass (eqn (5)), charge (eqn (6)) and momentum (eqn (7)) equations respectively. In eqn (5)–(7), the subscript 'j' denotes the indices of all the beads that are in the broken part of the jet.

$$m_i = \sum_j m_j, \tag{5}$$

$$q_i = \sum_j q_j,\tag{6}$$

$$m_i v_i = \sum_i m_j v_j, \tag{7}$$

The equations of motion for these droplets are also obtained from Newton's second law of motion. The forces acting on the beads are the aerodynamic drag force $(F_{d,i})$, the electric field force $(F_{e,i})$ and the gravitational force $(F_{g,i})$. The viscoelastic and surface tension forces are not included in eqn (8) as we assume that the droplets are rigid spheres.

$$m_i \frac{\mathrm{d}^2 x_i}{\mathrm{d}t^2} = F_{\mathrm{d},i} + F_{\mathrm{e},i} + F_{\mathrm{g},i},$$
 (8)

The air drag force on the droplets is given considering flow on a sphere. For bead 'i' of radius r_i the drag force is given in eqn (9) where V_{re} is the relative velocity of the air with respect to the droplet i.

$$F_{d,i} = \frac{C_{D}\pi r_{i}^{2}}{2} \rho_{air} V_{re,i} |V_{re,i}|,$$
 (9)

The drag coefficient C_D (eqn (10)) is obtained from the shear stress acting on the surface of the sphere. 31 The shear stress is calculated from the velocity profile of the surrounding air on a tiny boundary layer around the surface of the sphere.

$$C_{\rm D} = \frac{24}{{\rm Re}_{\rm air}} \left(1 + 0.1104 \sqrt{{\rm Re}_{\rm air}} \right)^2,$$
 (10)

The above equation is valid for $Re_{air} < 5000$ where $Re_{air} =$ $\rho_{\rm air} | V_{{\rm re},i} | d_i / \mu_{\rm air}$ with $\rho_{\rm air}$ being the density of air, $\mu_{\rm air}$ the viscosity of air and d_i the diameter of the droplet.

The electric force acting on the droplets is similar to eqn (2); however, the coulombic interactions between the droplets and the surface charges of the jet are also responsible for the total electric field force. The details on the implementation and procedure of the discretized modeling to electrically driven jets can be found in previous publications. 16,17,24

Results and discussion

In this section, we studied the spraying process of PVA/H₂O solution and the effect of air flow and voltage is observed. As we used a viscoelastic polymer solution in the experiments, the jet extends due to viscoelastic stress under driving force and then breaks into droplets. The spray process is different for fluids which are not viscoelastic. For non-viscoelastic fluids, the droplets are formed in the nozzle itself due to the atomization of the meniscus (Taylor cone).

In Sections 4.1 and 4.2, the radius of the droplets and the size distribution is obtained for three cases: (i) electrospray, (ii) air spray and (iii) air controlled (AC) electrospray. The radius of the droplets obtained from simulations for these three cases is compared with the experimental results. However, the simulation results provide an average radius of the droplets, but the size distributions of the droplets are not obtained. Later, in Section 4.3 the effect of air flow on the surface morphology and the yield of the AC electrospray are studied. The surface morphology formed from the AC electrospray of the solution of graphene oxide dispersion in water, a non-viscoelastic fluid, is studied. Finally, in Section 4.4, the three spray processes are applied to coat cathodes for lithium sulfur batteries and the electrochemical performance of these batteries is studied.

4.1 Electrospray and air spray

The experimental conditions used in this section are mentioned in Section 2.1. The electrospray process is studied at 3 different applied voltage differences. The electric field causes extension of the jet from the Taylor cone and axisymmetric instability acts on the extended jet. There are two modes of axisymmetric instabilities: the capillary mode and the conducting mode. 16,17 In the capillary mode of instability, the instability grows due to high and low pressure regions caused due to the modulations in the radius of the jet. 16 The low pressure region has a larger radius compared to the high pressure region as capillary pressure is inversely proportional to the radius of the jet. As the liquid travels from high pressure to low pressure, the region with a larger radius keeps growing and the region with a lower radius keeps shrinking and finally causes the jet to break-up. However in the conducting mode, the modulations on the jet surface lead to modulations on the surface charges of the jet. The coulombic interactions between these surface charges increase the instability and lead to the jet break-up. In highly conducting polymers, the conducting mode plays a dominant

Soft Matter Paper

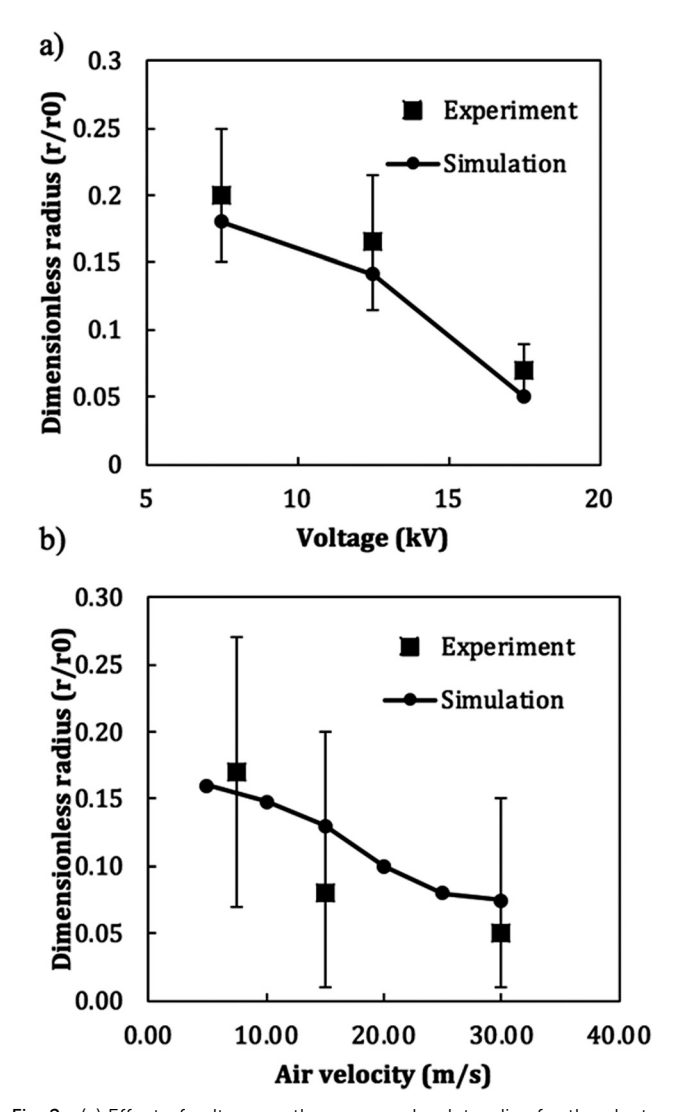


Fig. 2 (a) Effect of voltage on the average droplet radius for the electrospray process and (b) effect of air velocity on the average droplet radius for the air spray process

role in the instability growth rate. With an increase in the electric field, both the capillary pressure and the surface charges of the jet increase due to the formation of thin jets because of jet extension. 17 As the capillary pressure and surface charges are responsible for the jet break-up phenomenon, the increase in the electric field leads to an increase in the growth rate of the instability. Therefore, at higher voltages the droplet formation is more rapid, resulting in the formation of a large number of droplets. Also, the formation of thin jets at high voltage leads to smaller size droplets.

In the electrospray process, the jet length is short and the breakup occurs near the Taylor cone region. Also, from Fig. 2a, the size of the droplets is more consistent as observed from the standard deviation in the droplet size distribution. However, relatively few droplets are formed with the electrospray process. From Fig. 2a, we can observe that the radius of the droplets obtained from experiments is comparable to the simulation results.

The experimental result in the air spray case is obtained without applying any voltage difference between the nozzle and the collector. The solution is ejected out of the nozzle at a flow rate of 0.01 ml min⁻¹ and the air flow is applied coaxially to the jet. The drag force is mainly responsible for the extension of the jet. In this case, as there is no electric field, there is only the capillary mode of instability and the drag force further accelerates the instability growth rate. The effect of air flow on the droplet size distribution is studied for 3 different air flow rates. From Fig. 2b, we can observe that the size of the droplets decreases with the increase in air flow due to the formation of thin jets at high air flow rates. Also, the number of droplets increases with air flow as the instability growth rate also increases with the air flow rates. We also observed that compared to the electrospray process the number of droplets is much higher and the spraying process is more chaotic and rapid in the air spray case. In addition, the droplets formed are not of uniform size in the air spray case as seen from the standard deviation plot in Fig. 2b. From the experimental result for 50 m s⁻¹ air flow rate, we observe that there are multiple jets formed at the nozzle. However, in the simulations, we assume that only a single jet is ejected out of the nozzle.

4.2 Air controlled (AC) electrospray

The AC electrospray process is the combination of the electrospray (Section 4.1) and air spray (Section 4.1) processes. The droplet size is more uniform in the AC electrospray process compared to the air spray case due to the application of electric field (Fig. 3 and 4). The number of droplets increases with air flow as observed in the air spray case. Therefore, we can observe that the electric field is responsible for the uniformity of the droplets and the air flow is responsible for the formation of a large number of droplets. Also, the mean radius reduces as the air flow increases and the size of the droplets reduces by 65% under the effect of air flow compared to the no air flow case. We also observe that at a higher air flow rate, at 15 m $\rm s^{-1}$, the Taylor cone deforms and ejects multiple jets.

4.3 Controlling coating topology, morphology and nanoparticle dispersion via AC electrospraying

The surface roughness of the PVA/H₂O spray is measured by atomic force microscopy (Fig. 5a-c) for the AC electrospray process at 5 different air flow rates. From Fig. 5d, for a lower range $(0-15 \text{ m s}^{-1})$ of air flow rates, with an increase in air flow, there is a decrease in surface roughness. However, at a higher air flow rate, at 60 m s⁻¹, the surface roughness is increased. The initial decrease in surface roughness is due to the decrease in the size of the droplets sprayed on the substrate as observed in the AC electrospray case (Section 4.2). However, at 60 m s⁻¹ the spray is dry by the time it hits the surface of the collector, because of which the droplets make a rough coating on the substrate.

The coating efficiency of the spray is also measured for the AC electrospray process at 5 different air flow rates (Fig. 6). The coating efficiency is calculated from the ratio of the weight of the coating on the substrate and the weight of the polymer in

Paper Soft Matter

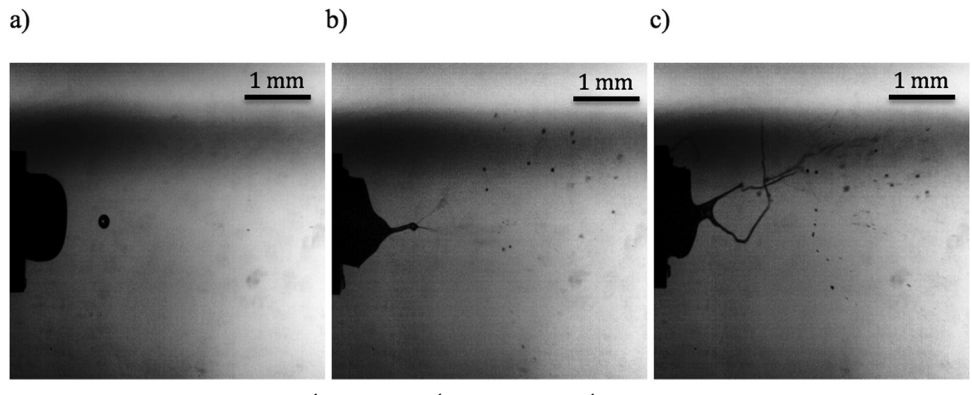


Fig. 3 Air controlled electrospray at air flow (a) 0 m s⁻¹, (b) 7.5 m s⁻¹ and (c) 15 m s⁻¹.

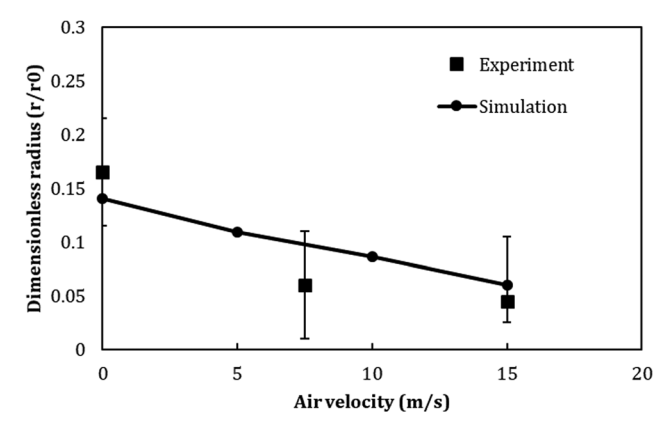


Fig. 4 Effect of air flow on the average droplet radius for the air controlled electrospray process.

the spinning solution as given in eqn (11). The coating efficiency increases for air flow rates of 0–15 m s⁻¹ due to larger deposition, as the air flow carries the droplets axially towards the substrate. However, at higher air flow rates the coating efficiency is reduced because of loss in the spray material as the direction of the spray is very non-axisymmetric and chaotic.

Coating efficiency (%) =
$$\frac{\text{weight of the spray coating}}{\text{weight of the polymer}} \times 100\%$$
, (11)

Carbon black is added to the PVA solution to investigate the macro-, micro-, and nano-scale morphologies of the PVA-CB coating deposited via the AC electrospraying process at different air flows (Fig. 7). It is evident from the SEM images (Fig. 7) that there is a significant deviation in the size distribution of droplets that are sprayed via conventional electrospray (Fig. 7a), ranging from 300 μ m (macro-scale) to 50 nm (nanoscale). The solvent evaporation is not precisely controlled in conventional electrospray, which results in deposition of solid polymer particles on the surface, creating rough topology. It can be observed in Fig. 7b–d, that with the application of the air flow in AC electrospray, the morphology and topology have significantly improved at all magnifications, due to precise control over atomization and a significant decrease in the droplet dimensions. It is important

to mention that the number of solid polymer particles on coating surfaces significantly decreased with the increase of the air flow (Fig. 7c and d). The polymer droplets are effectively directed towards the substrate by the air flow, and therefore, the final solvent evaporation takes place on the surface upon deposition. Extremely high assisting flows result in the premature solidification of the droplet, due to forced convection, increasing the number of solid particles on the surface of the coating (Fig. 7d). Therefore, AC electrospray can be effectively utilized to precisely control topology and morphology even at the nano scale. This is particularly useful for the development of superhydrophobic coatings, where the control of the surface roughness plays a crucial role and determines wetting angles. 1-3

The AC electrospray of PVA-CB can afford an electrically conductive coating due to the high electrical conductivity of the carbon powder. However, carbon black cannot be sprayed directly and needs to be sprayed with PVA which acts as a binder to stick to the substrate. In addition, graphene oxide is electrically conductive and can form uniform coatings using the AC electrospray process without the use of PVA (or any binder). Graphene oxide dispersion in water can directly be used to coat the copper (Cu) substrate using the AC electrospray process. This solution is non-polymeric, unlike PVA/H₂O solution that is used in the experiments discussed in Sections 4.1-4.3. The graphene oxide sheets undergo folding under external forces and therefore, the morphology of the spray surface can provide an insight into the droplet formation. When there is no air flow, the spray is very non-uniform and forms discrete particles from the SEM image (Fig. 8). However, with the application of the air flow rate, the spray forms a film on the substrate. In addition, with an increase in the air flow rate, the spray forms fewer wrinkles and a smoother morphology is observed (Fig. 8). Furthermore, from the SEM image of the cross-section of the sprayed material, there are no layers formed under no air flow conditions. However, layers can be observed when the air flow rate is applied on the spray and the layers are more densely packed in the 100 m s⁻¹ air flow case. This shows that the high air flow rate increases the rate of solvent evaporation of the spray yielding a dry layer of the coating on the substrate before another layer is coated. The layered structure of graphene oxide has been used to fabricate conductive and mechanically stable Soft Matter Paper

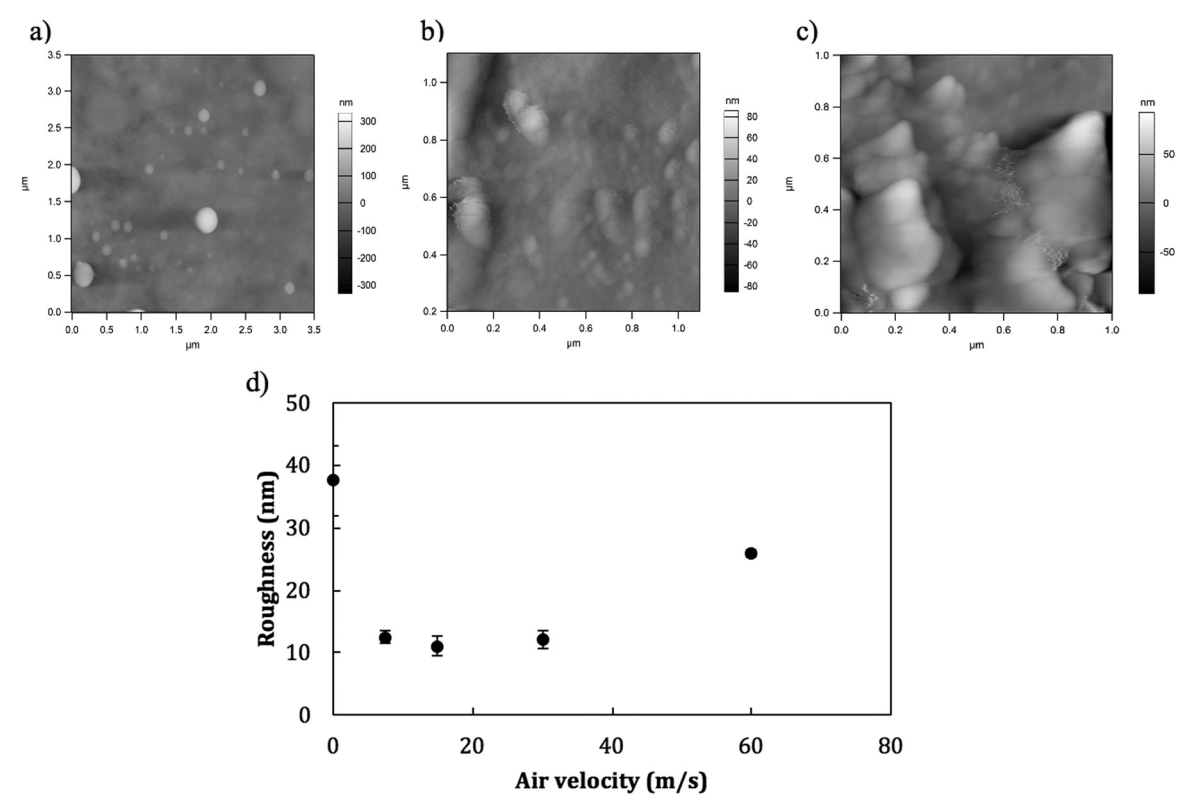


Fig. 5 AFM images of the AC electrospray surface of PVA/H₂O at air flow (a) 0 m s⁻¹ (b) 15 m s⁻¹ (c) 60 m s⁻¹ and (d) effect of air flow on surface roughness of the coating.

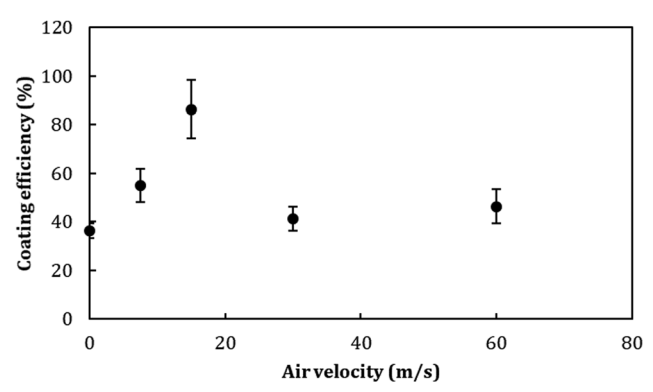


Fig. 6 Effect of air flow on coating efficiency of the AC electrospray of PVA/H2O

electrodes in batteries. The multi-layered structure can provide structural integrity and can accommodate large volume changes during the lithiation or delithiation process.

Lithium sulfur battery performance with air controlled electrospray coated electrodes

Li-S batteries are a promising candidate for the next generation of energy storage due to their high theoretical capacity and low cost.40,41 However, they need to overcome challenges like the highly insulating nature of sulfur and volume expansion in the battery during discharging. Thus, effective reaction site, conductive pathway, and mechanical stability are necessary to increase the utilization of sulfur. Therefore, in this section, a uniform coated cathode is fabricated using the AC electrospray process to improve the capacity and retention of Li-S batteries.

Fig. 9 shows the SEM images of the slurry coating, air spray, electrospray, and air controlled electrospray. For the slurry coated electrode (Fig. 9a), the surface image shows a dense layer with several cracks due to discrete grain boundaries formed during the drying process. The size of the cracks is observed to increase with the sulfur loading and electrode thickness. 42 In the spray techniques (Fig. 9b-d), the morphology highly depends on parameters such as flow rate, distance, electric field, and convective air flow. In Fig. 9b, the electrospray surface is dense consisting of inconsistent dark and light color regions. However, air spray electrodes show a more uniform coating as shown in Fig. 9c. Furthermore, by combining both, a more porous surface is obtained by air controlled electrospray. The voids and rough surfaces are beneficial as they can accommodate the sulfur expansion and also can enhance the electrolyte uptake. 43 We also note that the porosity of the electrode prepared by air-controlled electrospray with graphene/sulfur filled carbon mixture solution can be controlled by air flow, as shown in Fig. 8. The typical tap density of the electrode by air-controlled electrospray ranges between 0.2 g cm⁻³ and 0.6 g cm⁻³, while that prepared by slurry cast is about 0.4 g cm^{-3} which is similar to the value reported by Li et al.44

The electrochemical performance of lithium sulfur batteries is measured using four different coated electrodes: (i) slurry coating, (ii) electrospray - only electric field, (iii) air spray - only

Paper Soft Matter

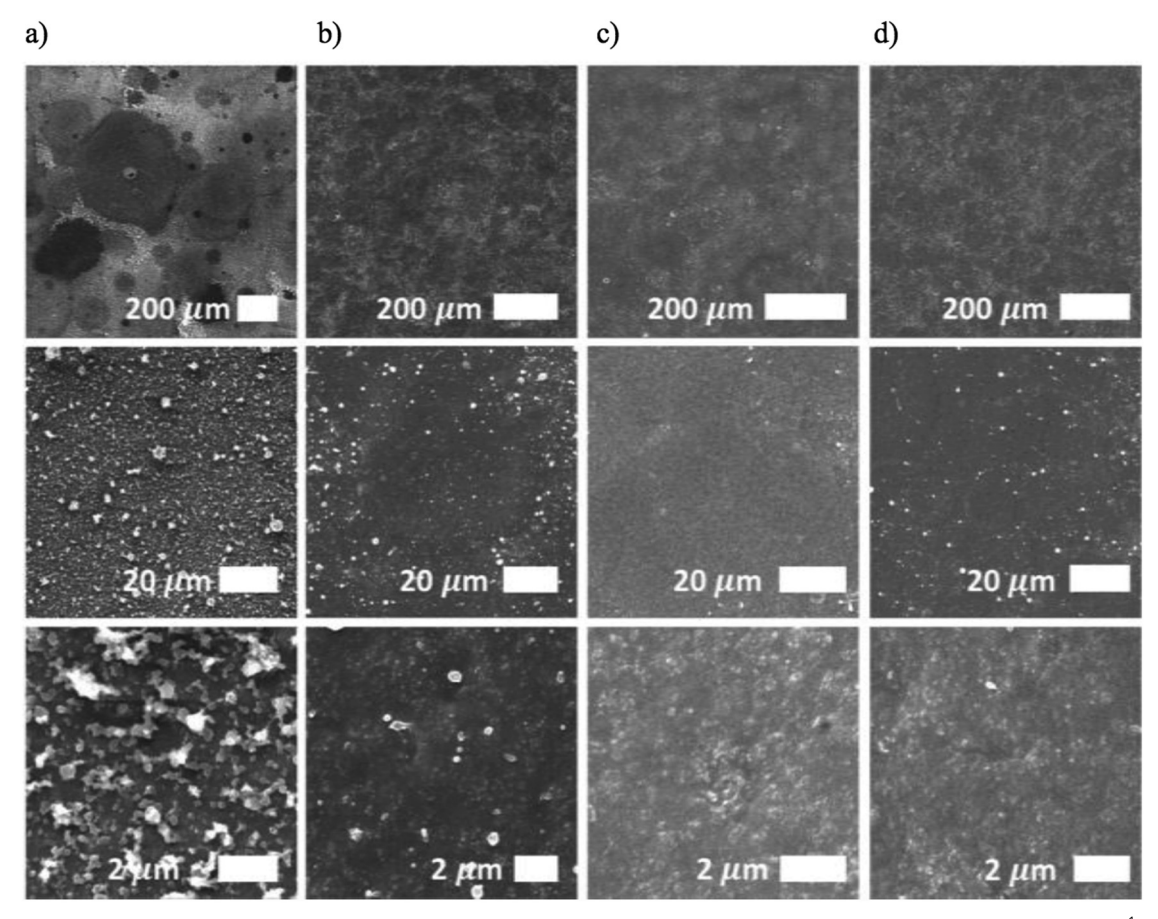


Fig. 7 SEM images of the macro/micro/nano-topology of 3% PVA solution with CB (15 vol% to PVA) coatings deposited via (a) 0 m s⁻¹, (b) 30 m s⁻¹, (c) 55 m s⁻¹ and (d) 70 m s⁻¹ sheath layer air flow AC electrospray.

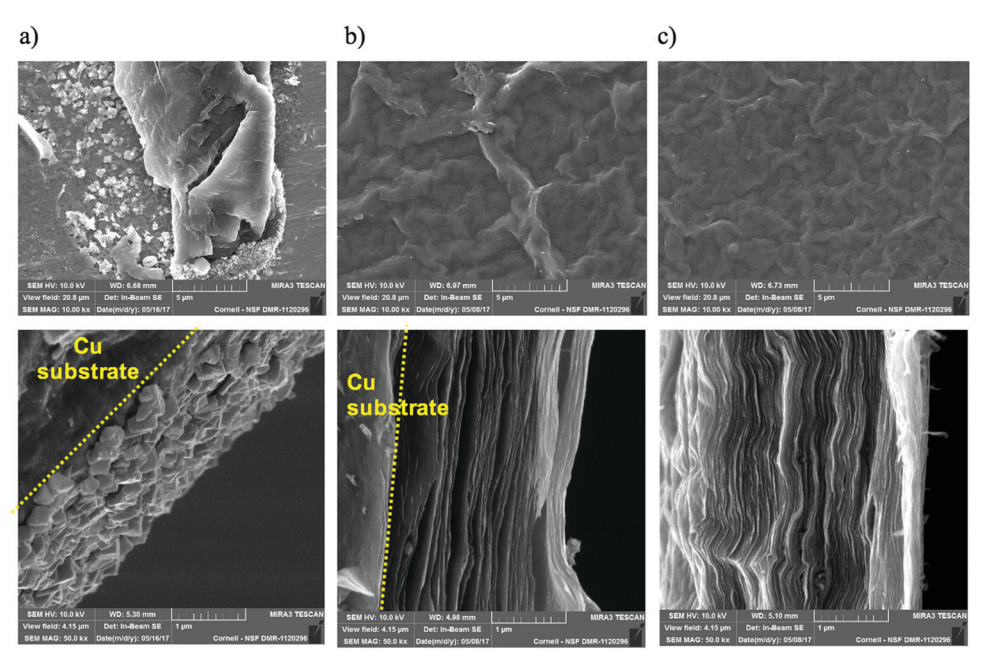
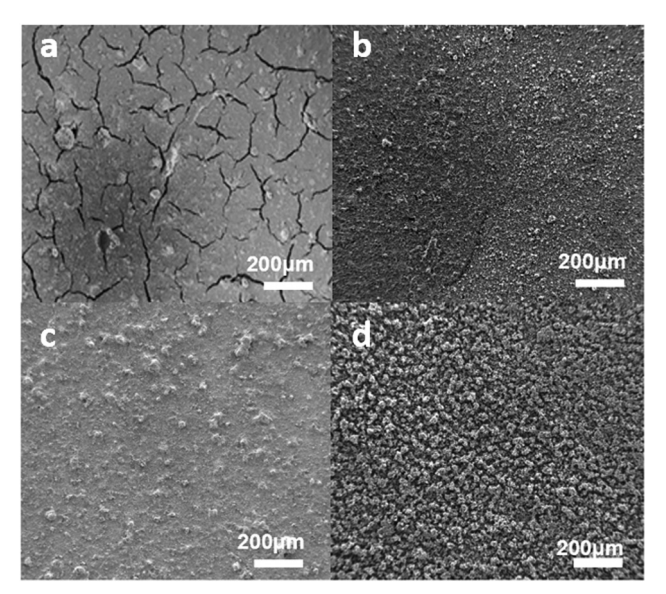


Fig. 8 Surface morphology and cross-section of the air controlled electrospray of GO at air flow (a) 0 m s^{-1} , (b) 50 m s^{-1} and (c) 100 m s^{-1} .

air, and (iv) air controlled electrospray – both air and electric field. In Fig. 10a, the discharge capacity of the electrode coated

by air controlled electrospray is higher than the only air and only electric field cases. The higher number of porous micro-size

Soft Matter Paper



SEM images of cathodes via (a) slurry coating, (b) electrospray (c) air spray and (d) air controlled electrospray.

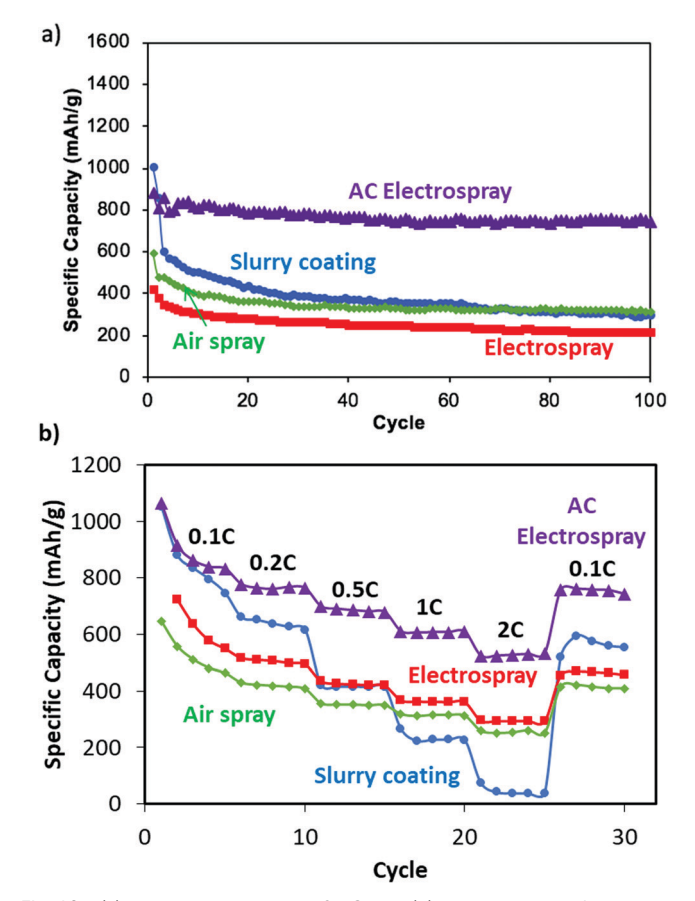


Fig. 10 (a) Discharge capacity at 0.5C, and (b) rate capability of the lithium sulfur battery cathode fabricated by air controlled electrospray, air spray and electrospray

structures formed in both air and electric field cases provides well-developed pathways to facilitate redox electron transfer and reduce interfacial resistance. It allows a higher conversion rate of lithium polysulfide to favorable chemical compounds for charge storage. Compared to slurry coating electrodes, elimination of cracks largely increases the mechanical stability, which further results in improved capacity retention.

The rate capability of cells at different C-rates is shown in Fig. 10b. As expected, the results followed a similar trend to cyclability. The difference in discharge capacities between the sprayed and slurry coating cells is even more evident at high current densities because the redox reaction kinetics are more significant at high current densities. At a C-rate of 2C, the air controlled electrospray cell still maintained 49.9% of its initial capacity, while the retention of the slurry coating cathode is only 7.2%. A discharge capacity of 756.8 mA h g⁻¹ is recovered after returning to 0.1C for air controlled electrospray.

5. Conclusions

The spray behavior of a viscoelastic polymer solution (PVA/H₂O) in air spray, electrospray, and air controlled electrospray cases is studied using simulations and experiments. A discretized model with the bead-spring approach is used for the simulations. The droplet formation from the jet break-up due to axisymmetric instability growth is studied from the model. The average radius of the droplets from simulations is compared with that in the experiments. The experimental observations are done by flow visualization using a high-speed camera and the droplet size distributions for the three spray cases are measured. The electric field is responsible for increasing the uniformity in the droplet size and the air flow rate is responsible for forming a large number of droplets. However, the size of the droplets reduced with the increase in both the applied electric field and the air flow rate. The surface roughness of the AC electrospray material measured by AFM is observed to decrease for the lower range $(0-15 \text{ m s}^{-1})$ of the applied air flow rate but the surface roughness increased at a high air flow rate (60 m s⁻¹). Furthermore, for the PVA system, we observe a significant improvement in the spatial distribution of carbon black active nano-inclusions in the coatings with an increase in the applied air flow. The air controlled electrospray of the graphene oxide/water system formed a smoother spray with packed distinct layers at a high air flow rate (100 m s⁻¹). The AC electrospray process is used to fabricate uniformly coated Li-S cathodes. The air controlled electrospray coated electrodes demonstrated improved capacity, retention and rate capability. The well-developed structure is efficient not only in providing conductive pathways for sulfur utilization but also for trapping polysulfides.

Conflicts of interest

There are no conflicts to declare.

Acknowledgements

This work was partly funded by the Battery 500 Seedling Program of the Energy Efficiency & Renewable (EERE) Office in U.S. Department

Paper Soft Matter

of Energy (DE-EE0008193). This work made use of the Cornell Center for Materials Research Shared Facilities which are supported through the NSF MRSEC program (DMR-1719875).

References

- 1 E. Burkarter, C. K. Saul, F. Thomazi, N. C. Cruz, L. S. Roman and W. H. Schreiner, Surf. Coat. Technol., 2007, 202, 194-198.
- 2 J. Bravo, L. Zhai, Z. Wu, R. E. Cohen and M. F. Rubner, Langmuir, 2007, 23, 7293-7298.
- 3 S. T. Yohe and M. W. Grinstaff, Chem. Commun., 2013, 49, 804-806.
- 4 Q. Guo, J. P. Mather, P. Yang, M. Boden and P. T. Mather, PLoS One, 2015, 10, 1-14.
- 5 L. T. De Jonge, S. C. G. Leeuwenburgh, J. J. J. P. Van Den Beucken, J. G. C. Wolke and J. A. Jansen, Adv. Funct. Mater., 2009, 19, 755-762.
- 6 M. Valvo, E. García-Tamayo, U. Lafont and E. M. Kelder, I. Power Sources, 2011, 196, 10191-10200.
- 7 C. H. Chen, E. M. Kelder, M. J. G. Jak and J. Schoonman, Solid State Ionics, 1996, 86, 1301-1306.
- 8 L. Wang, H. W. Xu, P. C. Chen, D. W. Zhang, C. X. Ding and C. H. Chen, J. Power Sources, 2009, 193, 846-850.
- 9 M. Yamashita and B. J. Fenn, J. Phys. Chem., 1984, 88, 4451-4459.
- 10 J. B. Fenn, M. Mann, C. K. Meng, S. F. Wong and C. M. Whitehouse, Science, 1989, 246, 64-71.
- 11 G. I. Taylor, Proc. R. Soc. London, Ser. A, 1964, 280, 383-397.
- 12 G. I. Taylor, Proc. R. Soc. London, Ser. A, 1965, 291, 145-158.
- 13 G. I. Taylor, Proc. R. Soc. London, Ser. A, 1969, 313, 453-475.
- 14 A. L. Yarin, S. Koombhongse and D. H. Reneker, J. Appl. Phys., 2011, 90, 4836-4846.
- 15 L. Rayleigh, Proc. R. Soc. London, 1879, 10, 473.
- 16 C. P. Carroll and Y. L. Joo, J. Non-Newtonian Fluid Mech., 2008, 153, 130-148.
- 17 C. P. Carroll and Y. L. Joo, Phys. Fluids, 2009, 21, 103101.
- 18 M. J. Divvela and Y. L. Joo, J. Appl. Phys., 2017, 121, 134306.
- 19 A. F. Spivak, Y. A. Dzenis and D. H. Reneker, Mech. Res. Commun., 2000, 27, 37-42.
- 20 D. H. Reneker, A. L. Yarin, H. Fong and S. Koombhongse, J. Appl. Phys., 2000, 87, 4531-4547.
- 21 M. M. Hohman, M. Shin, G. Rutledge and M. P. Brenner, Phys. Fluids, 2001, 13, 2201.
- 22 J. J. Feng, J. Non-Newtonian Fluid Mech., 2003, 116, 55-70.

- 23 C. P. Carroll and Y. L. Joo, Phys. Fluids, 2006, 18, 053102.
- 24 M. J. Divvela, L. M. Shepherd, M. W. Frey and Y. L. Joo, 3D Printing and Additive Manufacturing, 2018, vol. 5, pp. 248-256.
- 25 A. L. Yarin, Free Liquid Jets and Films: Hydrodynamics and Rheology, Longman Scientific & Technical and Wiley & Sons, Harlow, New York, 1993.
- 26 P. P. Bhat, S. Appathurai, M. T. Harris, M. Pasquali, G. H. McKinley and O. A. Basaran, Nat. Phys., 2010, 6, 625.
- 27 J. Grifoll and J. R. Llompart, J. Aerosol Sci., 2012, 47, 78-93.
- 28 C. B. Collado, G. Vidal-de-Miguel and P. M.-L. Sinues, Sens. Actuators, B, 2016, 223, 217-225.
- 29 C. P. Carroll and Y. L. Joo, J. Appl. Phys., 2011, 109, 094315.
- 30 M. J. Divvela, A. C. Ruo, Y. Zhmayev and Y. L. Joo, J. Non-Newtonian Fluid Mech., 2017, 247, 62-77.
- 31 F. F. Abraham, Phys. Fluids, 1970, 13, 2194-2195.
- 32 Y. Zhmayev, S. Pinge, G. Shoorideh, G. L. Shebert, P. Kaur, H. Liu and Y. L. Joo, Small, 2016, 12, 5543-5553.
- 33 S. H. Liao, C. C. Weng, C. Y. Yen, M. C. Hsiao, C. C. M. Ma, M. C. Tsai, A. Su, M. Y. Yen, Y. F. Lin and P. L. Liu, J. Power Sources, 2010, 195, 263-270.
- 34 D. V. Kosynkin, W. Lu, A. Sinitskii, G. Pera, Z. Sun and J. M. Tour, ACS Nano, 2011, 5, 968-974.
- 35 D. Duft, T. Achtzehn, R. Müller, B. A. Huber and T. Leisner, Nature, 2003, 421, 128.
- 36 V. Kalra, F. Escobedo and Y. L. Joo, J. Chem. Phys., 2010, 132, 24901.
- 37 M. R. Bockstaller, R. A. Mickiewicz and E. L. Thomas, Adv. Mater., 2005, 17, 1331-1349.
- 38 G. A. Buxton and A. C. Balazs, Phys. Rev. E: Stat., Nonlinear, Soft Matter Phys., 2003, 67, 031802.
- 39 A. K. Khandpur, S. Forster, F. S. Bates, I. W. Hamley, A. J. Ryan, W. Bras, K. Almdal and K. Mortensen, Macromolecules, 1995, 28, 8796-8806.
- 40 N. Deng, W. Kang, Y. Liu, J. Ju, D. Wu, L. Li, B. S. Hassan and B. Cheng, J. Power Sources, 2016, 331, 132-155.
- 41 A. Manthiram, Y. Fu and Y.-S. Su, Acc. Chem. Res., 2013, 46, 1125-1134.
- 42 Z. W. Seh, W. Li, J. J. Cha, G. Zheng, Y. Yang, M. T. McDowell, P. C. Hsu and Y. Cui, Nat. Commun., 2013, 4, 1331.
- 43 P. Barai, A. Mistry and P. P. Mukherjee, Extrem. Mech. Lett., 2016, 9, 359-370.
- 44 M. Li, Y. Zhang, F. Hassan, W. Ahn, X. Wang, W. W. Liu, G. Jiang and Z. Chen, J. Mater. Chem. A, 2017, 5, 21435.